Optik - International Journal for Light and Electron Optics 230 (2021) 166332

Contents lists available at ScienceDirect

Optik

journal homepage: www.elsevier.com/locate/ijleo

Original research article

Fixed-size double-resonant nanolaminate plasmonic nanoantennas with wide spectral tunability and high optical cross-sections

Yizhou Qian [1], Seied Ali Safiabadi Tail [1], Elieser Mejia, Wei Zhou *

Department of Electrical and Computer Engineering, Virginia Tech, Blacksburg, Virginia, 24061, USA

ARTICLE INFO

Keywords:
Plasmonics
Spectral tunability
Double-resonant
Mode overlapping
Multifunction

ABSTRACT

Plasmonic nanoantennas can support localized surface plasmon (LSP) modes to concentrate light at the nanoscale. Although "single-resonant" plasmonic nanoantennas are sufficient for applications based on single-photon processes, "double-resonant" or "multiresonant" plasmonic nanoantennas are more favorable for multiphoton nonlinear processes or wavelength-multiplexing multifunctional operations. Despite significant efforts, current multiresonant plasmonic nanoantennas still face challenges in achieving wide spectral tunability and high excitability for multiple LSP modes under strict geometric size-footprint constraints. Here, we propose and numerically demonstrate that fixed-size nanolaminate plasmonic nanoantennas (NLPNAs) consisting of multiple metal/insulator layers can support two highly excitable LSP modes with electrical dipole (ED) and magnetic dipole (MD) characteristics. Notably, the resonant wavelength of both ED and MD modes are broadly tunable in the near-infrared range between ~700 nm and ~1000 nm by controlling the thickness ratio between individual metal and insulator layers without changing the overall size. While the ED mode in NLPNAs can have large scattering cross-sections suitable for applications based on plasmonic emission/scattering processes, the MD mode has large absorption cross-sections desirable for applications based on plasmonic photothermal effects. We further reveal that NLPNAs' broad double-resonance tunability originates from the out-of-plane geometric dependence of the elementary ED/MD modes in the building blocks and their optical coupling.

1. Introduction

By supporting localized surface plasmon (LSP) modes, plasmonic nanoantennas based on metal-dielectric nanostructures can trap and concentrate light at the nanoscale to enhance both linear and nonlinear optical processes for various applications in areas ranging from information technology to energy and healthcare [1–6]. Due to the short LSP lifetimes (2–10 fs), the plasmon energy localized in nanoantennas depletes quickly through radiative decay pathways as free-space photons and nonradiative decay pathways as local heating [7–9]. In general, the use of relatively brighter LSP modes is advantageous for plasmonic enhancement of elastic/inelastic scattering and emission processes in applications, such as scattering based biosensing/bioimaging, surface-enhanced Raman spectroscopy (SERS), fluorescence spectroscopy, and nonlinear optics light sources [4,5,10–12]. On the other hand, using relatively darker LSP modes is preferable for nanolocalized photothermal heating processes in applications, such as solar energy photothermal

* Corresponding author.
E-mail address: wzh@vt.edu (W. Zhou).
[1] Co-First Authors Share Equal Contributions.

https://doi.org/10.1016/j.ijleo.2021.166332
Received 11 December 2020; Received in revised form 15 January 2021; Accepted 16 January 2021
Available online 22 January 2021
0030-4026/© 2021 Elsevier GmbH. All rights reserved.

conversion, photothermal cancer therapy, and photothermal neural activation [6,13–15]. Most previous studies focus on "single--resonant" plasmonic nanoantennas with optimized near-field and far-field optical characteristics (e.g., resonant wavelengths, near-field enhancement factors, optical cross-sections, and radiative/nonradiative decay rates), which are sufficient for applications based on single-photon excitation/emission/absorption processes. Nevertheless, by supporting two or more LSP modes, double-resonant or multiresonant plasmonic nanoantennas are more favorable for applications involving multiphoton nonlinear processes or wavelength-multiplexing multifunctional operations [16–18].

Although plasmonic antennas with larger dimensions can support multiple higher-order modes [19–21], higher-order modes typically have poor excitability by free-space light due to their dark multipolar nature. Different higher-order modes' resonant wavelengths cannot be tuned independently by geometric engineering due to their standing wave nature. Another approach to building multiresonant plasmonic nanoantennas is to incorporate multiple plasmonic resonators into a coupled system [22–25], which has limitations of large device footprints and complicated design/fabrication. Also, core-shell plasmonic nanoantennas can support multiple LSP modes by plasmon hybridization at multiple metal-dielectric interfaces [26–29]; however, it is challenging to independently tune individual modes in core-shell systems and to control core-shell geometries accurately in scalable fabrication.

Most multiresonant nanoantenna designs do not consider strict geometrical constraints in size, footprint, and shape. Nevertheless, some emerging applications at the nano-bio interface require multiresonant plasmonic nanoantennas with a fixed size/footprint/shape and a broad spectral tunability in near-infrared (NIR) wavelengths. First, using fixed-size nanodevices can maintain a consistent nano-bio interface with cells and cellular systems across separate experiments [30–34]. Second, the scalable nanofabrication of fixed-footprint and broadly-tunable nanoantennas is desirable for seamless integration with predefined nanoelectronics devices in the electrical-optical multimodal platforms [35–37]. Third, multiresonant nanoantennas can enable wavelength-multiplexed nanoscale multifunctionality at the nano-bio interface, for example, by simultaneously achieving SERS biochemical sensing and photothermal cellular activation under two laser sources at different wavelengths [16]. Finally, for many in-vivo biomedical applications, multi-resonant nanoantennas should support multiple LSP modes with tunable resonant wavelengths in the NIR biological window (NIR-I: 700–900 nm, NIR-II: 1000–1350 nm, and NIR-III: 1550–1870 nm) to benefit from deeper light penetration in tissues [38–40].

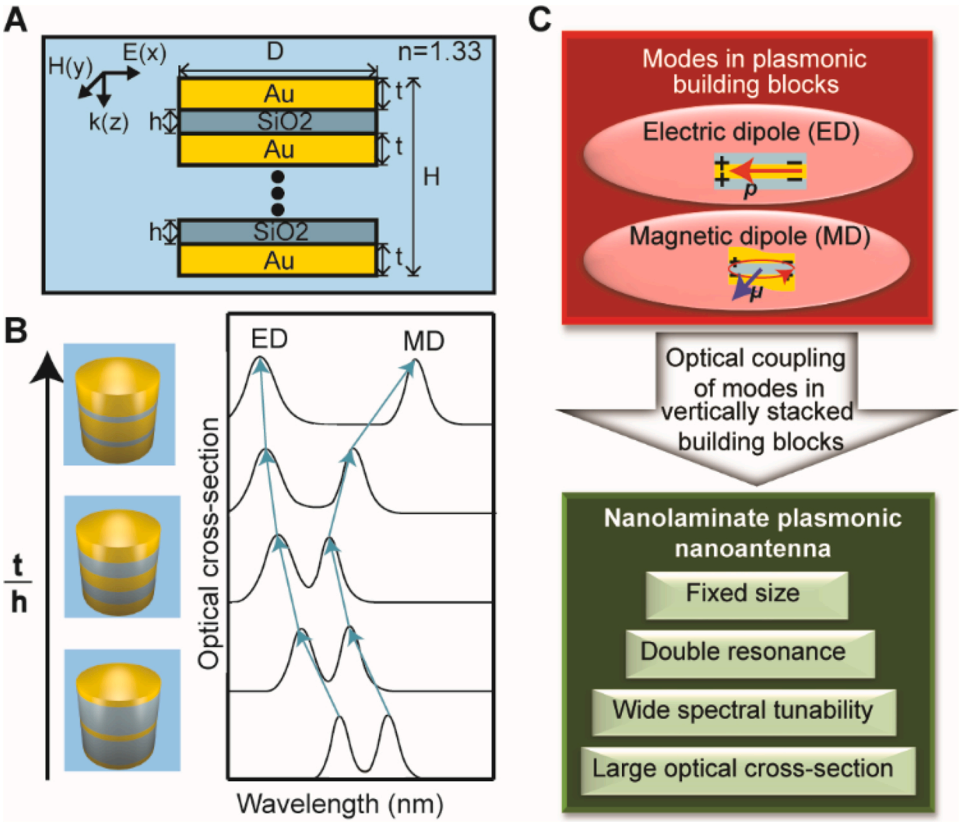

Fig. 1. Fixed-size double-resonant NLPNAs. (A) Cross-sectional schematic of a fixed-size nanolaminate plasmonic nanoantenna with a fixed-diameter (D) and a fixed-height (H) in water ($n = 1.33$) under x-polarized normal incident light. The nanolaminate plasmonic nanoantenna consists of alternating layers of Au thickness (t) and SiO_2 thickness (h) nanodisks. (B) Schematic illustration of the evolution of resonant wavelengths for hybridized electric dipole (ED) and magnetic dipole (MD) modes in a fixed-size nanolaminate plasmonic nanoantenna at different Au-SiO_2 thickness ratios (t/h). (C) Scheme of the mode hybridization strategy for engineering the double-resonant optical properties of fixed-size NLPNAs. NLPNAs consist of two types of plasmonic building blocks in the vertical stack, which are the insulator-metal-insulator (IMI) nanostructures, supporting the electric dipole (ED) modes, and the metal-insulator-metal (MIM) nanostructures, supporting the magnetic dipole (MD) modes.

In this work, we report that fixed-size nanolaminate plasmonic nanoantennas (NLPNAs) consisting of alternating metal and insulator nanodisks in a vertical stack can support two types of highly excitable LSP modes with electrical dipole (ED) and magnetic dipole (MD) characteristics (Fig. 1A), respectively. Notably, the resonant wavelengths of ED and MD modes are broadly tunable in the NIR range by controlling the thickness ratio between individual metal (t) and insulator (h) layers without changing the NLPNA's overall shape and size (diameter: D, and height: H) (Fig. 1B). Numerical simulations are performed by Finite-Difference-Time-Domain method (Ansys Inc.), and details are listed in Table S1 and Supporting Information. Furthermore, we find that the ED mode in NLPNAs tends to have large scattering cross-sections desirable for applications leveraging plasmonic emission/scattering processes, and the MD hybridized mode tends to have large absorption cross-sections desirable for applications leveraging plasmonic photothermal effects. Numerical simulations and analysis reveal that NLPNAs' double-resonance tunability originates from the out-of-plane geometric dependence of the elementary ED and MD modes in their insulator-metal-insulator (IMI) and metal-insulator-metal (MIM) building blocks (Fig. 1C). Furthermore, due to the intimate vertical stacking of IMI and MIM building blocks, the optical coupling strength among elementary ED and MD modes in IMI and MIM building blocks can be significantly changed by controlling the metal-to-insulator thickness ratio (t/h) in NLPNAs. The proposed plasmonic NLPNAs' geometries can be realized by the electron-beam evaporation of alternating metal and insulator thin films through nanohole array deposition masks [41,42], allowing nanometer-scale thickness accuracy in out-of-plane geometric engineering of plasmonic double-resonance properties.

2. Results and discussion

2.1. The effects of the metal layer thickness on the ED mode in an IMI building block

For understanding the effects of t/h variation on double-resonant properties of fixed-size NLPNAs, it is crucial to study the dependence of elementary ED and MD modes on the metal (Au, Johnson and Christy [43]) and insulator ($n = 1.5$) layer thicknesses in IMI and MIM building blocks. We first investigate the effects of varying t on the optical properties of an IMI building block. In an IMI building block, the two elementary ED modes at the two-constituent metal-insulator interfaces can interact through the middle metal layer, which has a negative real part of the permittivity ε . Therefore, as shown in Fig. 2A, an IMI plasmonic building block can support a low-energy bonding ED mode and a high-energy anti-bonding electric quadrupole (EQ) mode by the in-phase and out-of-phase coupling between the two elementary ED modes, respectively [44]. The splitting energy (ΔE) between the ED and the EQ modes increases with the coupling strength between the elementary ED modes and decreases with t. Compared with the low-energy bonding ED mode with a significant radiative decay rate, the high-energy EQ mode is subradiant and cannot effectively interact with free-space light due to its zero net ED moment and weak MD moment [45].

Fig. 2B depicts the calculated absorption and scattering spectra of an Au nanodisk in water (refractive index $n = 1.33$) with different t ranging from 4 nm to 40 nm. With a small t of 4 nm, the Au nanodisk shows a distinct resonance peak around ~980 nm due to the ED oscillations of free electrons in Au, and the absorption loss dominates over the scattering loss. As t increases from 4 nm to 16 nm, 28 nm, and 40 nm, the Au nanodisk's ED mode shows a monotonous blueshift of the resonant wavelength with reduced

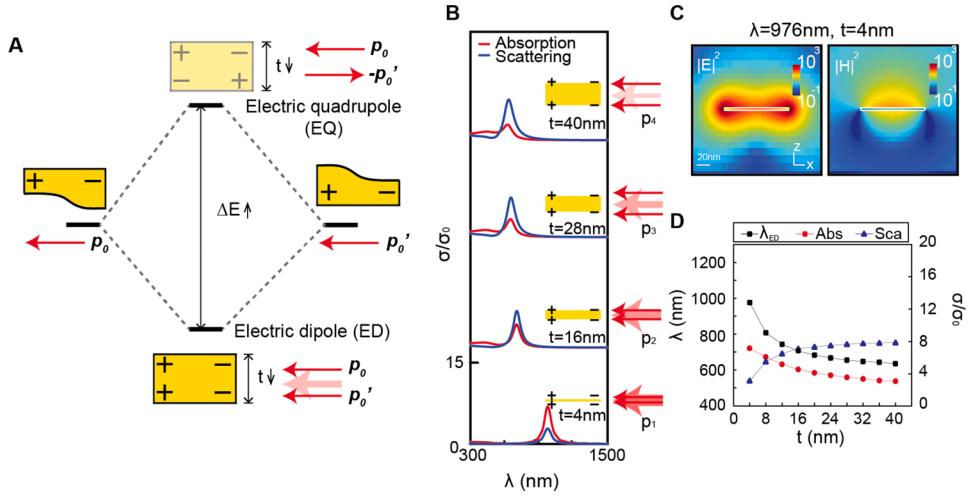

Fig. 2. Spectral tunability of the ED mode in an IMI building block by controlling the metal layer thickness (t). (A) Energy diagram illustration of ED mode and electric quadrupole (EQ) mode in an IMI nanodisk by the optical coupling between the elementary ED modes at the two metal-insulator interfaces with varying metal layer thicknesses (t). (B) FDTD-calculated spectra of normalized absorption and scattering cross-sections for an Au nanodisk in water ($n = 1.33$) with different Au layer thicknesses of 4, 16, 28, and 40 nm. σ_0 is the geometric cross-section of the nanodisk. (C) FDTD-calculated $|E|^2$ and $|H|^2$ at the resonant wavelength of the ED mode ($\lambda_{ED} = 976$ nm) for an Au nanodisk ($t = 4$ nm) in water ($n = 1.33$). (D) The dependence of the resonant wavelength (λ_{ED}) and the peak absorption/scattering cross-sections for the ED mode of an Au nanodisk in water ($n = 1.33$) on the Au thickness (t).

absorption and increased scattering. Additionally, as t increases, a broad absorption peak emerges around the wavelength ranging between 350 nm and 500 nm with an increased amplitude due to the electronic interband transition in Au. In Fig. 2C, the calculated distribution maps of $|E|^2$ and $|H|^2$ at the resonant wavelength for a thin Au nanodisk ($t = 4$ nm) can reveal the ED characteristics, where the electric field has a dipolar distribution in the plane of nanodisk and the magnetic field is circulating the induced ED oscillating current in the Au nanodisk.

In Fig. 2D, we plot the ED mode resonant wavelength and the peak absorption/scattering cross-sections as a function of t. As t increases from 4 nm to 16 nm, the resonant wavelength of ED mode blueshifts swiftly from ~980 nm to ~705 nm; however, as t further increases from 16 nm to 40 nm, the resonant wavelength of the ED mode slightly blueshifts from ~705 nm to ~636 nm. Such blueshifting is due to the reduced near-field optical coupling strength between elementary ED modes and reduced ΔE (Fig. 2A). The nonlinear dependence of resonant wavelength shifts of the ED mode on t originates from the optical fields of the elementary plasmonic ED modes exponentially decaying from the Au nanodisk metal-insulator interfaces into the metal. Therefore, only for a small metal thickness ($t < 16$ nm), a strong near-field optical coupling between elementary ED modes can occur to induce the plasmonic mode hybridization and thus a highly sensitive t dependence of ΔE between bonding and anti-bonding modes [46].

Fig. 2D shows that the relative contribution between scattering (σ_{sca}/σ_0) and absorption (σ_{abs}/σ_0) in the total optical loss for the ED mode also depends strongly on the thickness of the Au nanodisk, where σ_0 is the geometric cross-section of the nanodisk, σ_{sca} and σ_{abs} are the scattering and absorption cross-sections at the resonant wavelength. As t increases from 4 nm to 16 nm and 40 nm, σ_{sca}/σ_0 of the ED mode increases from ~2.8 to ~7.2 and ~7.6, while its σ_{abs}/σ_0 decreases from ~6.9 to ~4.8 and ~2.8. The increase in σ_{sca}/σ_0 is mainly due to the increased total number of free-moving charges in the Au nanodisk, resulting in increased resonant polarizability and increased radiative decay rate. On the other side, the decrease in σ_{abs}/σ_0 for the ED mode with t is mainly due to a gradual shift of t away from the critical coupling condition. Here, by normalizing the optical cross-sections by universal dipolar absorption limitation [47,48]:

$$\sigma/\sigma_k = \sigma/(3\pi/2k^2),$$

Where σ is the optical cross-section and k is the wavenumber in free space. The critical coupling condition occurs at $t = 8$ nm, whereby the frequency-normalized absorption reaches the maximum by matching with the scattering (Fig. S1A, Supporting Information).

2.2. The effects of the insulator gap layer thickness on the MD mode in a MIM building block

Next, we study the effects of h on the optical response of the MIM plasmonic building block composed of optically thick metal layers. In such a system, the elementary ED modes at the two metal-insulator interfaces couple with each other through the middle insulator layer, which has a positive permittivity ε (Fig. 3A), resulting in a high-energy anti-bonding ED mode from the in-phase coupling of the elementary ED modes and a low-energy bonding EQ mode from the out-of-phase coupling of the elementary ED modes [45,49]. Due to the formation of an oscillating current loop consisting of both conduction current in metal layers and displacement current in the insulator gap, the low-energy EQ mode also exhibits MD characteristics, capable of being excited by

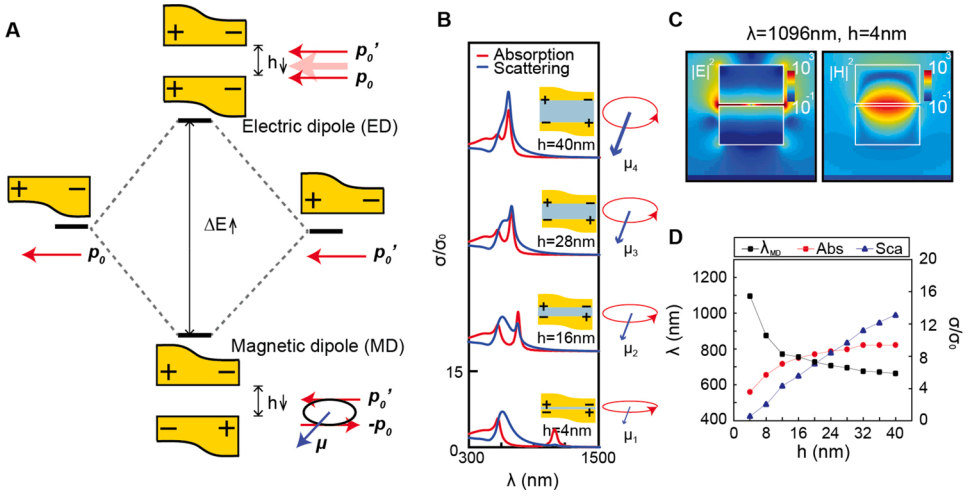

Fig. 3. Spectral tunability of the MD mode in a MIM building block by controlling the insulator gap layer thickness (h). (A) Energy diagram illustration of ED mode and MD mode in a MIM nanodisk by the optical coupling between the elementary ED modes at the two metal-insulator interfaces with varying insulator layer thicknesses (h). (B) FDTD-calculated spectra of normalized absorption and scattering cross-sections for an Au-SiO_2-Au nanodisk in water ($n = 1.33$) with different SiO_2 ($n = 1.5$) thicknesses (h) of 4, 16, 28, and 40 nm and a fixed Au thickness (t) of 60 nm. (C) FDTD-calculated distribution maps of $|E|^2$ and $|H|^2$ at the resonant wavelength of the MD mode ($\lambda_{MD} = 1096$ nm) for an Au-SiO_2-Au nanodisk ($t = 60$ nm, and $h = 4$ nm) in water (n = 1.33). (D) The dependence of the resonant wavelength (λ_{MD}) and the peak absorption/scattering cross-sections (σ_{abs}/σ_0 and σ_{sca}/σ_0) for the MD mode of an Au-SiO_2-Au nanodisk ($t = 60$ nm) in water (n = 1.33) on the insulator (SiO_2) thickness (h).

free-space light and thus is referred to as the MD mode.

As shown in the calculated σ_{abs}/σ_0 and σ_{sca}/σ_0 spectra of a MIM building block (Fig. 3B), the resonant wavelengths of the low-energy MD mode and high-energy ED mode strongly depend on h. For $h = 4$ nm, due to the strong optical coupling between the elementary ED modes, the high-energy ED mode at ~600 nm and low-energy MD mode at ~1100 nm exhibit the most significant ΔE. The calculated distribution maps of $|E|^2$ and $|H|^2$ can illustrate the MD nature of the unperturbed gap mode with a three-order enhancement of $|E|^2$ and a two-order enhancement of $|H|^2$ within the nanogap (Fig. 3C). The increase of h from 4 nm to 40 nm reduces the optical coupling strength between the top and bottom Au disks' elementary ED modes and the MD mode resonant wavelength blueshifts due to a reduced ΔE. As h approaches 40 nm, the low-energy MD mode can largely overlap with the high-energy ED mode to have significantly increased absorption due to their near-field interactions.

Fig. 3D depicts the effects of h variations on the optical responses of the MD mode. By increasing h from 4 to 16 nm and 40 nm, the MD mode resonant wavelength first blueshifts rapidly from 1100 nm to 770 nm, and then blueshifts gradually from 770 nm to 670 nm. Also, as h increases from 4 nm to 40 nm, σ_{sca}/σ_0 increases continuously from ~0.5 to ~13.1, manifesting the gradually increased MD moment strength due to an expanded current loop area. In contrast, as h increases from 4 nm to 24 nm and 40 nm, σ_{abs}/σ_0 first increases rapidly from ~3.6 to ~8.2 and then saturates by reaching the critical coupling condition at $h = 24$ nm (Fig. S1B). It is crucial to note that the ED mode off-resonantly contributes to the absorption at the MD mode resonant wavelength and breaks the single dipolar absorption limit [47,50,51].

2.3. The effects of the metal layer thickness on ED and MD modes in a MIM building block

As the metal (Au) layer thickness in a MIM building block is comparable to or smaller than the optical skin depth, the elementary ED modes at all four insulator-metal interfaces can interact with each other (Fig. 4A). Such a MIM building block can be treated as two optically coupled IMI subsystems in the vertical stack (Fig. 4A), supporting a high-energy ED and a low-energy MD mode from the in-phase and out-of-phase coupling between the elementary ED modes in the two IMI subsystems. Therefore, changing t affects the elementary ED modes of IMI subsystems and alters the overall optical response.

As shown in FDTD-calculated σ_{abs}/σ_0 and σ_{sca}/σ_0 (Fig. 4B), the optical response of a MIM building block with a fixed insulator gap thickness ($h = 8$ nm) can change significantly with reduced t from 40 nm to 4 nm. For $t = 4$ nm, the MIM unit only exhibits a high-energy anti-bonding ED mode with a high absorption cross-section; however, the low-energy bonding MD mode is absent since the small t can limit the current loop area to cause a weak coupling with free-space light. As t increases from 4 to 16, 28, and 40 nm, the ED mode blueshifts with increased σ_{sca}/σ_0 and reduced σ_{abs}/σ_0, while the emergent MD mode blueshifts with increased σ_{abs}/σ_0 due to an enlarged current loop area.

Fig. 4C shows the dependence of the ED mode resonant wavelength (λ_{ED}), σ_{sca}/σ_0 and σ_{abs}/σ_0 on t. With t increasing from 4 to 20 and 40 nm, λ_{ED} initially blueshifts swiftly from ~844 to ~660 nm and then gradually to ~620 nm. As t increases from 4 to 20 and 40 nm, σ_{abs}/σ_0 rapidly decreases from ~6.3 to ~3.0, and then gradually from ~3.0 to ~2.0, while σ_{sca}/σ_0 first rapidly increases from ~5.7 to ~8.1, and then slightly decreases from ~8.1 to ~7.8. Compared to the ED mode, the MD mode shows a very different dependence of

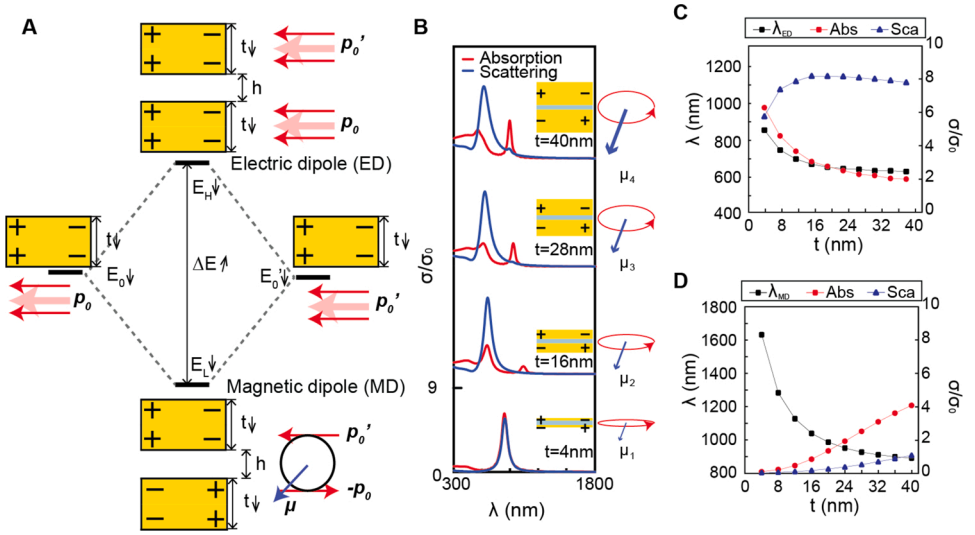

Fig. 4. Spectral tunability of ED mode and MD mode in a MIM building block by controlling the metal layer thickness (t). (A) Energy diagram illustration of ED mode and MD mode in a MIM nanodisk by the optical coupling between the elementary ED modes in the two metal nanodisks with varying metal layer thicknesses (t). (B) FDTD-calculated far-field spectra of absorption and scattering cross-sections for Au-SiO_2-Au nanodisks in water ($n = 1.33$) with different Au thicknesses (t) of 4, 16, 28, and 40 nm and a fixed SiO_2 ($n = 1.5$) thickness (h) of 8 nm. (C-D) The dependence of the resonant wavelength and the peak absorption/scattering cross-sections for (C) the ED mode and (D) the MD mode of an Au-SiO_2-Au nanodisk ($h = 8$ nm) in water (n = 1.33) on the Au thickness (t).

the resonant wavelength (λ_{MD}), σ_{sca}/σ_0 and σ_{abs}/σ_0 on t (Fig. 4D). As t increases from 4 to 20 and 40 nm, λ_{ED} first rapidly blueshifts from ~1630 to ~1000 nm and then gradually to ~900 nm. Unlike the ED mode, with increased t from 4 to 40 nm, σ_{abs}/σ_0 and σ_{sca}/σ_0 for the MD mode keep increasing from ~0.1 to ~4.1 and from ~0 to ~1.0, respectively, due to an increased effective loop area.

2.4. NLPNAs with different numbers of IMI and MIM building blocks

For NLPNAs consisting of multiple IMI and MIM building blocks, its optical response depends not only on the resonant properties of the elementary ED and MD modes but also on their mutual optical interactions. Fig. 5A-C depict the calculated σ_{abs}/σ_0 and σ_{sca}/σ_0 spectra for NLPNAs made of different numbers of metal (Au) and insulator (n = 1.5) layers, where t is 12 nm, h is 9 nm, and D is 100 nm. In agreement with the results of Fig. 4, the one-insulator-gap MIM system supports a dominant ED resonant peak at ~ 700nm and a weaker MD resonant peak at ~ 1152*nm* (Fig. 5A). Unlike the one-insulator-gap MIM system (Fig. 5A), the two-insulator-gap MIMIM (Fig. 5B) and three-insulator-gap MIMIMIM (Fig. 5C) systems manifest three resonant features, including the ED mode, MD mode, and an additional low-energy resonance. With an increased number of MIM building blocks in the vertical stack, the resonant wavelength of the ED mode slightly blueshifts from ~ 700*nm* (MIM) to ~ 684*nm* (MIMIM) and ~ 664*nm* (MIMIMIM); in contrast, the MD mode shows significantly blueshifted wavelengths from ~ 1152*nm* (MIM) to ~ 988*nm* (MIMIM) and ~ 868*nm* (MIMIMIM), and the resonant wavelength of the additional low-energy mode also blueshifts considerably from ~ 1264*nm* (MIMIM) to ~ 1076*nm* (MIMIMIM). The different dependence of mode resonant wavelength on the number of vertically stacked building blocks reflects the different mutual coupling strengths between elementary ED and MD modes in IMI and MIM building blocks. Remarkably, the absorption and scattering cross-sections of modes also strongly depend on the number of vertically stacked building blocks. With increased building block numbers, the ED mode absorption σ_{abs}/σ_0 decreases from ~3.82 (MIM) to ~3.1 (MIMIM) and ~2.8 (MIMIMIM) while its scattering σ_{sca}/σ_0 slightly increases from ~7.9 (MIM) to ~ 8.6 (MIMIM) and ~8.7 (MIMIMIM), revealing an increased total ED moment strength due to the increased total charge number. In contrast, the MD mode absorption σ_{abs}/σ_0 significantly increases from ~0.4 (MIM) to ~3.1 (MIMIM) and ~4.1 (MIMIMIM) and its scattering σ_{sca}/σ_0 slightly increases from ~0.02(MIM) to ~0.1 (MIMIM) and ~1.5 (MIMIMIM), revealing an increased total MD moment strength due to the larger current loop area.

To investigate the microscopic physics behind the far-field absorption and scattering responses for MIMIMIM NLPNAs, we calculated near-field distribution profiles of the electric and magnetic field intensities, $|E|^2$ and $|H|^2$, and the electric and magnetic field phase angles, $\phi(E_x)$ and $\phi(H_y)$, for the three resonant features at λ_1, λ_2, and λ_3 (Fig. 5D-F). Fig. 5D reveals that the mode profile for λ_1 mode consists of ED characteristics with a uniform $\phi(E_x)$ within the four individual Au disks and intense $|E|^2$ localized at the edges of individual Au disks. Besides, the λ_1 mode also shows magnetic quadrupole (MQ) characteristics with intense $|H|^2$ concentrated at the top and bottom surface of TNLNAs and an out-of-phase distribution of $\phi(H_y)$ separated at a middle Au nanodisk plane. As expected, the λ_2 mode exhibits MD characteristics with high magnetic fields $|H|^2$ and in-phase $\phi(H_y)$ across multiple metal and insulator layers within NLPNAs (Fig. 5E). Remarkably, the λ_2 mode can concentrate the high electric fields $|E|^2$ with an enhancement factor over 10^3 into the three insulator gaps of MIM building blocks. Besides, the λ_2 mode also exhibits electric quadrupole (EQ) characteristics with an out-of-phase distribution of $\phi(E_x)$ separated at a middle insulator nanodisk plane. Finally, the weakly excited λ_3 mode reveals (*i*)

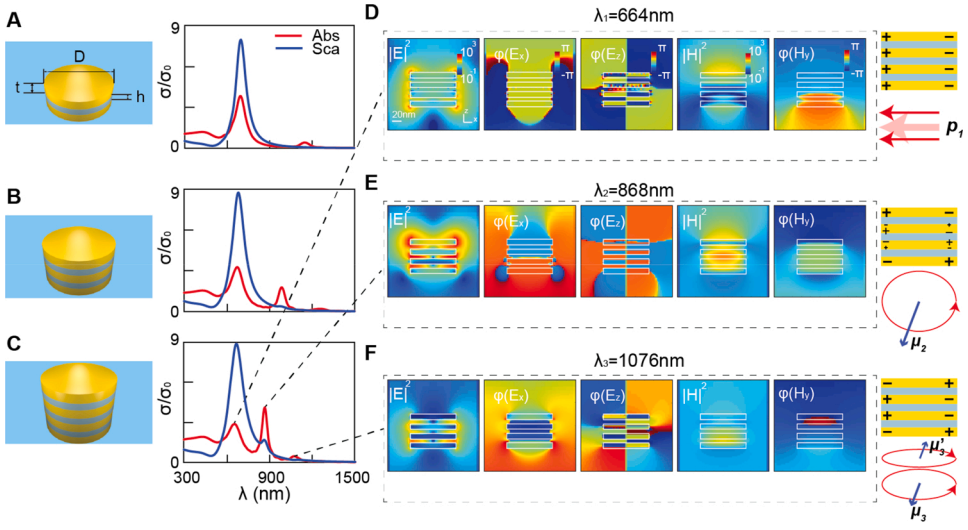

Fig. 5. Far-field and near-field optical properties of NLPNAs with different numbers of vertically stacked MIM building blocks. FDTD-calculated spectra of normalized absorption and scattering cross-sections for the NLPNAs in water ($n = 1.33$) with (A) one insulator layer, (B) two insulator layers, and (C) three insulator layers. The thickness of Au layers (t) is 12 nm, the thickness of SiO_2 layers (h) is 9 nm, and the diameter of the nanolaminate nanoantenna (D) is 100 nm. (D-F) FDTD-calculated distribution maps of $|E|^2$, $\phi(E_x)$, $\phi(E_z)$, $|H|^2$, and $\phi(H_y)$ for the modes of three insulator gap NLPNAs in water ($n = 1.33$), respectively, with (D) ED mode, (E) two MD mode, and (F) MQ mode.

magnetic quadrupole (MQ) characteristics with nearly out-of-phase $\phi(H_y)$ in the two MIM nanogaps but with the higher magnetic field $|H|^2$ and electric field $|E|^2$ concentrated in the bottom MIM nanogap, and (*ii*) electric high-order multipolar characteristics with out-of-phase $\phi(E_x)$ distributions among the top, the middle two, and the bottom Au nanodisks (Fig. 5F). The near-field distribution maps of the corresponding modes from bulk Au disk, one-insulator-gap MIM, and two-insulator-gap MIMIM systems show similar profiles (Fig. S2, Supporting Information). Besides, with a further increase in layer numbers, the MD mode absorption would eventually saturate due to the more substantial phase-retardation effect (Fig. S3, Supporting Information).

2.5. Effects of metal-to-insulator thickness ratio on double-resonant properties of NLPNAs

For the fixed-size MIMIM NLPNAs with varying t/h ratios (Fig. 6A), their σ_{abs}/σ_0 and σ_{sca}/σ_0 spectra always show two prominent resonant features: the ED mode at the lower wavelength and the MD mode at the higher wavelength. As t/h increases from 4 nm/44 nm to 28 nm/8 nm, the ED mode blueshifts from 918 nm to 621 nm in an increasingly saturated manner, similar to the behavior of single IMI building blocks (Fig. 2B). Furthermore, with increasing t/h, the ED mode absorption σ_{abs}/σ_0 rapidly decreases from ~7.7 to ~2.1 while its scattering σ_{sca}/σ_0 slightly increases from ~5.6 to ~7.8.

As shown in Fig. 6A, the MD mode shows a very different dependence of optical responses on t/h. As t/h increases from t_{4nm}/h_{44nm} to t_{20nm}/h_{20nm}, the resonant wavelength of the MD mode blueshifts from 1066 nm to 745 nm; however, as t/h further increases from t_{20nm}/h_{20nm} to t_{28nm}/h_{8nm}, the MD mode resonant wavelength reverses its shifting direction and redshifts from 745 nm to 850 nm. This unusual t/h dependence of MD resonant wavelength reflects a trade-off between two competing effects in NLPNAs consisting of multiple MIM and IMI building blocks. First, decreasing h can redshift the elementary MD modes in MIM building blocks due to the increased coupling strength between elementary ED modes in MIM building blocks and the increased ΔE (Fig. 3B). Such h modulation effects on the MD mode can become dominant for NLPNAs with thin insulator layers (h<20 nm). Second, increasing t blueshifts the elementary MD modes due to the elementary ED mode's blueshift in IMI building blocks (Fig. 4B). Such t modulation effects on the MD mode can become dominant for NLPNAs with thin metal layers (t<20 nm). Notably, although the MD mode resonant wavelength strongly depends on the t/h changes in NLPNAs, the resonant absorption of the MD mode sustains high values ($\sigma_{abs}/\sigma_0 > \sim 8$) due to several effects. First, since the MD mode in NLPNAs has the current loop area extending across the multiple MIM building blocks in the vertical stack, the MD moment strength becomes less sensitive to the t/h changes (Fig. 6B-D). Second, the ED mode in NLPNAs consisting of multiple IMI building blocks has an increased ED moment strength with a more considerable radiative decay broadening, which can interact with the MD mode through the near-field to enhance further the absorption of the MD mode (Fig. S6A, Supporting Information).

To investigate near-field optical properties for MD modes at various resonant wavelengths by changing t/h of NLPNAs, we plot MD mode distribution profiles of $|E|^2$, $\phi(E_x)$, $\phi(E_x)$, $|H|^2$, and $\phi(H_y)$ for two-insulator-gap NLPNAs with t_{28nm}/h_{8nm} (Fig. 6B), t_{16nm}/h_{26nm}

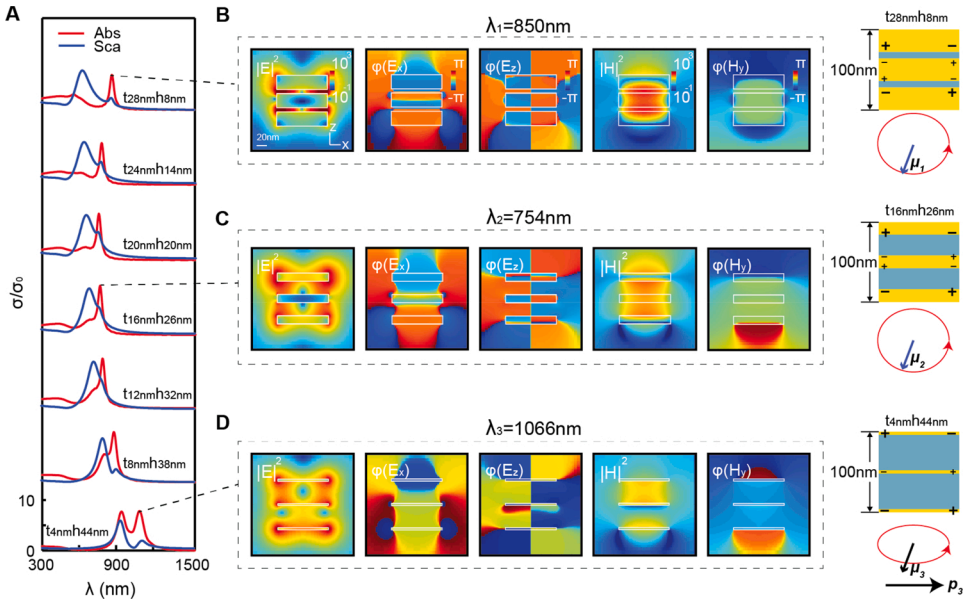

Fig. 6. Far-field and near-field optical properties of fixed-size MIMIM NLPNAs with different metal-to-insulator thickness ratios (t/h). (A) FDTD-calculated spectra of normalized absorption and scattering cross-sections for fixed-size Au-SiO_2-Au-SiO_2-Au nanoantennas in water ($n = 1.33$) with different thicknesses for Au (t) and SiO_2 (h) layers, which have the fixed diameter (D) and the height (H) of ~100 nm. (B-C) FDTD-calculated distribution maps of $|E|^2$, $\phi(E_x)$, $\phi(E_z)$, $|H|^2$, and $\phi(H_y)$ for the MD related modes of fixed-size Au-SiO_2-Au-SiO_2-Au nanoantennas with different thicknesses of Au and SiO_2 layers in water ($n = 1.33$), including (B) $t = 28$ nm and $h = 8$ nm, (C) $t = 16$ nm and $h = 26$ nm, and (D) $t = 4$ nm and $h = 44$ nm.

(Fig. 6C), and t_{4nm}/h_{44nm} (Fig. 6D). The distribution maps of $|E_x|^2$ and $|E_z|^2$ are provided in Fig. S4A and Supporting Information. First, for the t_{28nm}/h_{8nm} NLPNAs consisting of thin insulator layers (8 nm), the MD mode at $\lambda_1 = 850$ nm is spectrally far from the ED mode at 600 nm and can exhibit pure MD characteristics confining intense $|H|^2$ of in-phase $\phi(H_y)$ within the two MIM building blocks. Notably, a flat out-of-phase $\phi(E_x)$ distribution boundary cuts the center plane of the middle metal nanodisk, manifesting the two in-phase MD loop current oscillations in the two MIM building blocks. Second, for the t_{16nm}/h_{26nm} NLPNAs consisting of thicker insulator layers ($h = 26$ nm), the MD mode at $\lambda_2 = 750$ nm spectrally overlaps the broad ED mode at 680 nm and exhibits hybrid MD and ED characteristics in the near field, showing the less confined $|H|^2$ and extended $\phi(H_y)$ outside the two MIM building blocks. Furthermore, the out-of-phase $\phi(E_x)$ distribution boundary in the middle metal nanodisk shows a wavy profile due to an increased interfacial electron scattering perturbation to the conduction current $J_x = \sigma E_x$ in thinner metal disks, where σ is the conductivity in the metal. Finally, for the t_{4nm}/h_{44nm} NLPNAs made of ultrathin metal layers ($t = 4$ nm), the MD mode at $\lambda_2 = 1066$ nm has a spectral overlap with the broad ED mode at 950 nm; nevertheless, its near-field profiles show the MD characteristics in the top MIM building block and the ED characteristics in the bottom metal nanodisk. Remarkably, the out-of-phase $\phi(E_x)$ and J_x can no longer exist in the ultrathin middle metal nanodisk because the significant interfacial electron scattering makes it difficult to establish in-phase coupling of MD loop current oscillations in the two MIM building blocks. Such analysis is also consistent for 3-insulator-gap fixed-size NLPNAs (Figs. S4B, S5, S6B, Supporting Information)

Fig. 7 provides side-by-side comparisons of the t/h dependent double-resonance properties between one-insulator-gap (MIM), two-insulator-gap (MIMIM), and three-insulator-gap (MIMIMIM) NLPNAs with a fixed size ($D = 100$ nm, $H = 100$ nm). To assess the overall performance in the spectral tunability and resonant optical responses, the resonant wavelength λ_0, absorption σ_{abs}/σ_0, and scattering σ_{sca}/σ_0 are plotted as a function of metal-to-insulator thickness ratio t/h for both ED and MD modes in fixed-sized NLPNAs consisting of different numbers of metal and insulator layers.

For one-insulator-gap (MIM) fixed-sized NLPNAs (Fig. 7A), as t/h increases from 4 nm/92 nm to 12 nm/38 nm and 48 nm/4 nm, the ED mode resonant wavelength changes from ~930 nm to ~737 nm and ~613 nm, the ED mode absorption σ_{abs}/σ_0 changes from ~7.3 to ~6.3 and ~1.9, and the ED mode scattering σ_{sca}/σ_0 changes from ~3.52 to ~8.07 and ~8.42. On the other hand, with t/h increased from 4 nm/92 nm to 12 nm/38 nm, 28 nm/44 nm, and 48 nm/4 nm, the MD mode resonant wavelength changes from ~ 1100 nm to ~ 770 nm, ~697 nm and ~ 1107 nm, the MD mode absorption σ_{abs}/σ_0 changes from ~ 6.94 to ~11.35, ~9.98, and ~ 2.98, and the MD mode scattering σ_{sca}/σ_0 changes from ~ 0.95 to ~6.44, ~6.97 and ~ 0.38. These observations reveal several key points. First, the EM mode tends to induce larger scattering than absorption, while the MD mode tends to have larger absorption than the scattering. Second, the requirement of large ED mode scattering ($\sigma_{sca}/\sigma_0 > 8$) can limit the resonant wavelength tunability range ($\Delta\lambda_0 = \sim 68$ nm) of the ED mode between ~701 nm and ~633 nm. Third, the requirement of large MD mode absorption ($\sigma_{abs}/\sigma_0 > 8$) can limit the resonant wavelength tunability range ($\Delta\lambda_0 = \sim 176$ nm) of the MD mode between ~697 nm and ~873 nm.

For two-insulator-gap (MIMIM) fixed-sized NLPNAs (Fig. 7B), as t/h increases from t_{4nm}/h_{44nm} to t_{12nm}/h_{32nm} and t_{28nm}/h_{8nm}, the

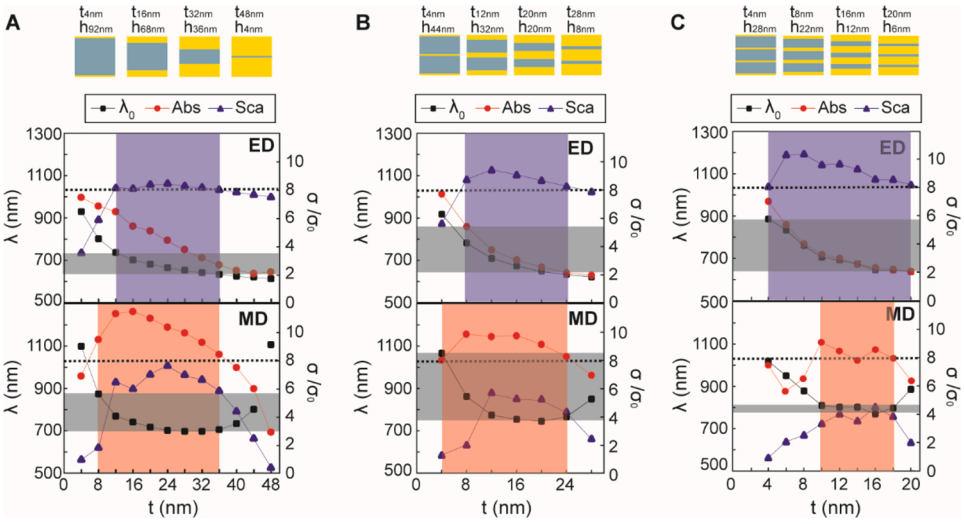

Fig. 7. Spectral tunability of fixed-size double-resonant NLPNAs with different numbers of vertically stacked MIM building blocks by controlling the metal-to-insulator thickness ratio (t/h). (A-C) The dependence of the resonant wavelength and the peak absorption/scattering cross-sections of the ED mode and the MD mode on the Au layer thickness (t) for fixed-size NLPNAs with (A) one insulator layer, (B) two insulator layers, and (C) three insulator layers, in water ($n = 1.33$). The diameter and the total height of NLPNAs with different numbers of Au-SiO_2-Au building blocks are fixed as ~100 nm. In the top panel of (A-C), the vertical shaded blue bands depict the range of Au layer thickness (t) for the ED mode with high peak scattering ($\sigma_{sca}/\sigma_0 \geq 8$), and horizontal shaded grey bands represent the tunable resonant wavelength range for a high scattering regime. In the bottom panel of (A-C), the vertical shaded red bands depict the range of Au layer thickness (t) for the MD mode with high peak absorption ($\sigma_{abs}/\sigma_0 \geq 8$), and horizontal shaded grey bands represent the tunable resonant wavelength range for the MD mode with the peak absorption $\sigma_{abs}/\sigma_0 \geq 8$ (For interpretation of the references to colour in this figure legend, the reader is referred to the web version of this article).

ED mode resonant wavelength changes from ~ 1066 nm to ~ 709 nm and ~ 621 nm, the ED mode absorption σ_{abs}/σ_0 changes from ~ 7.70 to ~ 3.74 and ~ 1.95, and the ED mode scattering σ_{sca}/σ_0 changes from ~ 5.58 to ~9.37 and ~ 7.84. On the other hand, with t/h increased from t_{4nm}/h_{44nm} to t_{8nm}/h_{42nm}, t_{20nm}/h_{20nm}, and t_{28nm}/h_{8nm}, the MD mode resonant wavelength changes from ~ 1066 nm to ~ 862 nm, ~ 745 nm and ~ 850 nm, the MD mode absorption σ_{abs}/σ_0 changes from ~ 7.98 to ~ 9.83, ~ 9.11, and ~6.93, and the MD mode scattering σ_{sca}/σ_0 changes from ~ 1.2 to ~ 1.95, ~ 5.19 and ~ 2.39. Compared to one-insulator-gap (MIM) NLPNAs, two-insulator-gap (MIMIM) NLPNAs can support both a high scattering ED mode ($\sigma_{sca}/\sigma_0 > 8$) with an increased resonant wavelength tunability range ($\Delta\lambda_0 = \sim$136 nm) between ~781 nm and ~645 nm, and a high absorption MD mode ($\sigma_{abs}/\sigma_0 > 8$) with an increased resonant wavelength tunability range ($\Delta\lambda_0 = \sim$321 nm) between ~745 nm to ~1066 nm.

For three-insulator-gap (MIMIMIM) fixed-sized NLPNAs (Fig. 7C), as t/h increases from t_{4nm}/h_{28nm} to and t_{10nm}/h_{20nm} and t_{20nm}/h_{6nm}, the ED mode resonant wavelength blueshifts from ~ 886 nm to ~ 705 nm and ~ 637 nm, the ED mode absorption σ_{abs}/σ_0 decreases from ~ 7.04 to ~3.27 and ~ 2.07, and the ED mode scattering σ_{sca}/σ_0 increases from ~ 8.06 to ~9.61 and gradually decreases to ~ 8.17. On the other hand, with t/h increased from t_{4nm}/h_{28nm} to t_{10nm}/h_{20nm} and t_{20nm}/h_{6nm}, the MD mode resonant wavelength changes from ~ 1018 nm to ~ 810 nm and ~ 886 nm, the MD mode absorption σ_{abs}/σ_0 changes from ~ 7.75 to ~9.22 and ~ 6.75, and the MD mode scattering σ_{sca}/σ_0 changes from ~ 0.90 to ~3.32 and ~ 1.98. Compared with two-insulator-gap (MIMIM) NLPNAs, the three-insulator-gap (MIMIMIM) NLPNAs show an improved resonant wavelength tunability ($\Delta\lambda_0 = \sim$249 nm, between 886 nm and 637 nm) to achieve the high-scattering ED mode ($\sigma_{abs}/\sigma_0 > 8$) but significantly reduced resonant wavelength tunability ($\Delta\lambda_0 = \sim$40 nm, between 769 nm and 809 nm) to achieve the high-absorption MD mode ($\sigma_{abs}/\sigma_0 > 8$). Therefore, the two-insulator-gap (MIMIM) fixed-sized NLPNAs exhibit the best performance to achieve t/h dependent double-resonance spectral tunability for the high-scattering ED mode and high-absorption MD mode.

3. Conclusion

In summary, our numerical studies show that fixed-sized NLPNAs can support highly excitable ED and MD modes with a broad spectral tunability by manipulating the metal-to-insulator thickness ratio (t/h). We reveal that the excellent double-resonance tunability of fixed-sized NLPNAs is due to the significant out-of-plane geometric dependence of the elementary ED modes in IMI building blocks, the elementary MD modes in MIM building blocks, and the coupling between elementary MD modes. We envision that fixed-sized NLPNAs with broad double-resonance tunability can enable wavelength-multiplexing plasmonics multifunctionality at the nano-bio interface. For example, it is possible to exploit double-resonant NLPNAs under laser sources at two different wavelengths for in-situ SERS biochemical monitoring of cellular activities [34,52] in response to the nanolocalized photothermal activation of electrogenic cells and cellular networks [53]. Besides, the integration of fixed-size double-resonant NLPNAs on the top of nanopillar nanoelectrodes can allow for hybrid optical-electrical multimodality at the nano-bio interface, such as bioelectrical recording of cellular action potentials [54,55], electrochemical sensing of biomolecules [56], SERS biochemical sensing, optical neural stimulation [57], and cell membrane optoporation [58].

Declaration of Competing Interest

The authors report no declarations of interest.

Acknowledgments

The authors gratefully acknowledge funding support from the Air Force Office of Scientific Research (AFOSR) Young Investigator AwardFA9550-18-1-0328 and National Institute of Standards and Technology (NIST) grants 70NANB18H201 and 70NANB19H163.

Appendix A. Supplementary data

Supplementary material related to this article can be found, in the online version, at doi:https://doi.org/10.1016/j.ijleo.2021.166332.

References

[1] J.A. Schuller, E.S. Barnard, W. Cai, Y.C. Jun, J.S. White, M.L. Brongersma, Plasmonics for extreme light concentration and manipulation, Nat. Mater. 9 (3) (2010) 193–204.
[2] L. Novotny, N. Van Hulst, Antennas for light, Nat. Photonics 5 (2) (2011) 83–90.
[3] A. Kinkhabwala, Z. Yu, S. Fan, Y. Avlasevich, K. Müllen, W. Moerner, Large single-molecule fluorescence enhancements produced by a bowtie nanoantenna, Nat. Photonics 3 (11) (2009) 654–657.
[4] J.N. Anker, W.P. Hall, O. Lyandres, N.C. Shah, J. Zhao, R.P. Van Duyne, Biosensing with plasmonic nanosensors. Nanoscience and Technology: a Collection of Reviews From Nature Journals, World Scientific, 2010, pp. 308–319.
[5] S.-Y. Ding, et al., Nanostructure-based plasmon-enhanced Raman spectroscopy for surface analysis of materials, Nat. Rev. Mater. 1 (6) (2016) 1–16.
[6] M.L. Brongersma, N.J. Halas, P. Nordlander, Plasmon-induced hot carrier science and technology, Nat. Nanotechnol. 10 (1) (2015) 25–34.
[7] S. Link, M.A. El-Sayed, Spectral Properties and Relaxation Dynamics of Surface Plasmon Electronic Oscillations in Gold and Silver Nanodots and Nanorods, ACS Publications, 1999.

[8] C. Voisin, N. Del Fatti, D. Christofilos, F. Vallée, Ultrafast Electron Dynamics and Optical Nonlinearities in Metal Nanoparticles, ACS Publications, 2001.
[9] C. Sönnichsen, et al., Drastic reduction of plasmon damping in gold nanorods, Phys. Rev. Lett. 88 (7) (2002) 077402.
[10] M. Pelton, Modified spontaneous emission in nanophotonic structures, Nat. Photonics 9 (7) (2015) 427–435.
[11] M. Kauranen, A.V. Zayats, Nonlinear plasmonics, Nat. Photonics 6 (11) (2012) 737–748.
[12] L. Bonacina, P.-F. Brevet, M. Finazzi, M. Celebrano, Harmonic generation at the nanoscale, J. Appl. Phys. 127 (23) (2020) 230901.
[13] G. Baffou, R. Quidant, F.J. García de Abajo, Nanoscale control of optical heating in complex plasmonic systems, ACS Nano 4 (2) (2010) 709–716.
[14] X. Huang, P.K. Jain, I.H. El-Sayed, M.A. El-Sayed, Plasmonic photothermal therapy (PPTT) using gold nanoparticles, Lasers Med. Sci. 23 (3) (2008) 217.
[15] P. Bazard, R.D. Frisina, J.P. Walton, V.R. Bhethanabotla, Nanoparticle-based plasmonic transduction for modulation of electrically excitable cells, Sci. Rep. 7 (1) (2017) 1–13.
[16] S.A.S. Tali, W. Zhou, Multiresonant plasmonics with spatial mode overlap: overview and outlook, Nanophotonics 8 (7) (2019) 1199–1225.
[17] H. Aouani, et al., Multiresonant broadband optical antennas as efficient tunable nanosources of second harmonic light, Nano Lett. 12 (9) (2012) 4997–5002.
[18] M. Celebrano, et al., Mode matching in multiresonant plasmonic nanoantennas for enhanced second harmonic generation, Nat. Nanotechnol. 10 (5) (2015) 412.
[19] E.K. Payne, K.L. Shuford, S. Park, G.C. Schatz, C.A. Mirkin, Multipole plasmon resonances in gold nanorods, J. Phys. Chem. B 110 (5) (2006) 2150–2154.
[20] E.-A. You, W. Zhou, J.Y. Suh, M.D. Huntington, T.W. Odom, Polarization-dependent multipolar plasmon resonances in anisotropic multiscale Au particles, ACS Nano 6 (2) (2012) 1786–1794.
[21] M. Kuttge, F.J. García de Abajo, A. Polman, Ultrasmall mode volume plasmonic nanodisk resonators, Nano Lett. 10 (5) (2010) 1537–1541.
[22] H. Harutyunyan, G. Volpe, R. Quidant, L. Novotny, Enhancing the nonlinear optical response using multifrequency gold-nanowire antennas, Phys. Rev. Lett. 108 (21) (2012) 217403.
[23] K. Thyagarajan, S. Rivier, A. Lovera, O.J. Martin, Enhanced second-harmonic generation from double resonant plasmonic antennae, Opt. Express 20 (12) (2012) 12860–12865.
[24] K. Thyagarajan, J.R.M. Butet, O.J. Martin, Augmenting second harmonic generation using Fano resonances in plasmonic systems, Nano Lett. 13 (4) (2013) 1847–1851.
[25] Y. Zhang, F. Wen, Y.-R. Zhen, P. Nordlander, N.J. Halas, Coherent Fano resonances in a plasmonic nanocluster enhance optical four-wave mixing, Proc. Natl. Acad. Sci. 110 (23) (2013) 9215–9219.
[26] H. Wang, D.W. Brandl, F. Le, P. Nordlander, N.J. Halas, Nanorice: a hybrid plasmonic nanostructure, Nano Lett. 6 (4) (2006) 827–832.
[27] R. Bardhan, S. Mukherjee, N.A. Mirin, S.D. Levit, P. Nordlander, N.J. Halas, Nanosphere-in-a-nanoshell: a simple nanomatryushka, J. Phys. Chem. C 114 (16) (2010) 7378–7383.
[28] S. Mukherjee, H. Sobhani, J.B. Lassiter, R. Bardhan, P. Nordlander, N.J. Halas, Fanoshells: nanoparticles with built-in Fano resonances, Nano Lett. 10 (7) (2010) 2694–2701.
[29] S. Hong, J.A. Acapulco Jr, H.Y. Jang, S. Park, Au nanodisk-core multishell nanoparticles: synthetic method for controlling number of shells and intershell distance, Chem. Mater. 26 (12) (2014) 3618–3623.
[30] A.F. McGuire, F. Santoro, B. Cui, Interfacing cells with vertical nanoscale devices: applications and characterization, Annu. Rev. Anal. Chem. 11 (2018) 101–126.
[31] M.E. Spira, A. Hai, Multi-electrode array technologies for neuroscience and cardiology, Nat. Nanotechnol. 8 (2) (2013) 83.
[32] A. Zhang, C.M. Lieber, Nano-bioelectronics, Chem. Rev. 116 (1) (2016) 215–257.
[33] J. Abbott, et al., CMOS nanoelectrode array for all-electrical intracellular electrophysiological imaging, Nat. Nanotechnol. 12 (5) (2017) 460–466.
[34] W. Nam, et al., Refractive-index-insensitive nanolaminated SERS substrates for label-free raman profiling and classification of living cancer cells, Nano Lett. 19 (10) (2019) 7273–7281.
[35] M. Dipalo, et al., Cells adhering to 3D vertical nanostructures: cell membrane reshaping without stable internalization, Nano Lett. 18 (9) (2018) 6100–6105.
[36] M. Dipalo, et al., Membrane poration mechanisms at the cell–nanostructure interface, Adv. Biosyst. 3 (12) (2019) 1900148.
[37] S.G. Higgins, M. Becce, A. Belessiotis-Richards, H. Seong, J.E. Sero, M.M. Stevens, High-aspect-ratio nanostructured surfaces as biological metamaterials, Adv. Mater. 32 (9) (2020) 1903862.
[38] K. Welsher, S.P. Sherlock, H. Dai, Deep-tissue anatomical imaging of mice using carbon nanotube fluorophores in the second near-infrared window, Proc. Natl. Acad. Sci. 108 (22) (2011) 8943–8948.
[39] M.-F. Tsai, et al., Au nanorod design as light-absorber in the first and second biological near-infrared windows for in vivo photothermal therapy, ACS Nano 7 (6) (2013) 5330–5342.
[40] P. Vijayaraghavan, C.H. Liu, R. Vankayala, C.S. Chiang, K.C. Hwang, Designing multi-branched gold nanoechinus for NIR light activated dual modal photodynamic and photothermal therapy in the second biological window, Adv. Mater. 26 (39) (2014) 6689–6695.
[41] J. Song, W. Zhou, Multiresonant composite optical nanoantennas by out-of-plane plasmonic engineering, Nano Lett. 18 (7) (2018) 4409–4416.
[42] J. Henzie, M.H. Lee, T.W. Odom, Multiscale patterning of plasmonic metamaterials, Nat. Nanotechnol. 2 (9) (2007) 549–554.
[43] P.B. Johnson, R.-W. Christy, Optical constants of the noble metals, Phys. Rev. B 6 (12) (1972) 4370.
[44] Y. Bian, Z. Zheng, X. Zhao, J. Zhu, T. Zhou, Symmetric hybrid surface plasmon polariton waveguides for 3D photonic integration, Opt. Express 17 (23) (2009) 21320–21325.
[45] J. Chen, G.A. Smolyakov, S.R. Brueck, K.J. Malloy, Surface plasmon modes of finite, planar, metal-insulator-metal plasmonic waveguides, Opt. Express 16 (19) (2008) 14902–14909.
[46] N.J. Halas, S. Lal, W.-S. Chang, S. Link, P. Nordlander, Plasmons in strongly coupled metallic nanostructures, Chem. Rev. 111 (6) (2011) 3913–3961.
[47] R. Alaee, M. Albooyeh, C. Rockstuhl, Theory of metasurface based perfect absorbers, J. Phys. D Appl. Phys. 50 (50) (2017) 503002.
[48] D.M. Pozar, Microwave Engineering, John wiley & sons, 2009.
[49] J. Dionne, L. Sweatlock, H. Atwater, A. Polman, Plasmon slot waveguides: towards chip-scale propagation with subwavelength-scale localization, Phys. Rev. B 73 (3) (2006) 035407.
[50] S. Tretyakov, Maximizing absorption and scattering by dipole particles, Plasmonics 9 (4) (2014) 935–944.
[51] N.M. Estakhri, A. Alu, Minimum-scattering superabsorbers," *physical review B*, vol. 89 (12) (2014) 121416.
[52] C. Zong, et al., Surface-enhanced Raman spectroscopy for bioanalysis: reliability and challenges, Chem. Rev. 118 (10) (2018) 4946–4980.
[53] J.L. Carvalho-de-Souza, J.S. Treger, B. Dang, S.B. Kent, D.R. Pepperberg, F. Bezanilla, Photosensitivity of neurons enabled by cell-targeted gold nanoparticles, Neuron 86 (1) (2015) 207–217.
[54] M. Dipalo, et al., Intracellular and extracellular recording of spontaneous action potentials in mammalian neurons and cardiac cells with 3D plasmonic nanoelectrodes, Nano Lett. 17 (6) (2017) 3932–3939.
[55] A. Habib, X. Zhu, U.I. Can, M.L. McLanahan, P. Zorlutuna, A.A. Yanik, Electro-plasmonic nanoantenna: a nonfluorescent optical probe for ultrasensitive label-free detection of electrophysiological signals, Sci. Adv. 5 (10) (2019) p. eaav9786.
[56] D. Zhang, et al., Nanoplasmonic biosensor: coupling electrochemistry to localized surface plasmon resonance spectroscopy on nanocup arrays, Biosens. Bioelectron. 67 (2015) 237–242.
[57] M. Dipalo, et al., Plasmonic meta-electrodes allow intracellular recordings at network level on high-density CMOS-multi-electrode arrays, Nat. Nanotechnol. 13 (10) (2018) 965–971.
[58] V. Caprettini, et al., Enhanced Raman investigation of cell membrane and intracellular compounds by 3D plasmonic nanoelectrode arrays, Adv. Sci. 5 (12) (2018) 1800560.